Bio-inspired 3D-printing of Layered Amorphous Calcium Carbonate Composites

Hadar Shaked [a], Daniela Dobrynin [a], Iryna Polishchuk [a], Alexander Katsman[a], Boaz Pokroy [a*]

(a) Department of Materials Science and Engineering and the Russell Berrie Nanotechnology Institute, Technion – Israel Institute of Technology, 32000, Haifa, Israel.

*Corresponding author, Email Address: bpokroy@technion.ac.il

Abstract

In nature, composites are often formed in the course of biomineralization, composed of a brittle mineral reinforcement joined by a ductile organic matrix. The formed composites often originate from an amorphous precursor such as amorphous calcium carbonate (ACC), and obtain a layered structure. In this study, we utilized robocasting, a 3D-printing technique to print models inspired by the *Ophiomastix wendtii* and the *Odontodactylus scyllarus* layered structures. We compared various bio-degradable organic matrices with a high percentage (>94%) of ACC reinforcements and studied their mechanical properties. With the organic matrix protection, ACC was stabilized for long periods of time, exceeding two years, when stored at ambient conditions. The layered models were printed and tested to evaluate their strength. The breakage interface was examined as well, to weigh the benefits an amorphous precursor may offer in 3D printing processes of ceramic materials. The breakage interface presented bulk behavior with no distinct layering, resembling the formation of single crystalline organs in nature, and overcoming one of the most burning problems in 3D printing, the layers' interfaces. Herein we present a bio-inspired, ecological formation of layered structures, resulting in a bulk material after low-temperature sintering, composed of stabilized ACC and biodegradable, environmentally friendly matrices.

Introduction

Biomineralization is the process through which organisms form minerals in nature. There are various pathways that organisms may choose to utilize in forming these biominerals. Some of these pathways include precipitation from saturated solutions, organic matrix-mediated mineralization, matrix vesicle mineralization, and amorphous-to-crystalline transformation.

[1,2] The presence of an amorphous precursor is notably common in the realm of calcium carbonate ($CaCO_3$), particularly in its metastable phase referred to as amorphous calcium carbonate (ACC).[3,4] The crystallization through ACC in nature facilitates the formation of mechanically strengthened and intricately shaped crystals in marine organisms. This process permits the incorporation of impurities at concentrations well beyond their thermodynamic limit of solubility. A commonly observed impurity in $CaCO_3$ biominerals is Mg, which can be incorporated at concentrations as high as 40 at.% [5,6], considerably surpassing its thermodynamic solubility of approximately 2 at.%.[7] Furthermore, it has been demonstrated that Mg plays a cardinal role in stabilizing ACC over extended durations, preventing its crystallization. In a recent study, we illustrated that ACC enriched with magnesium is stabilized over an extended period and can serve as an ink for 3D printing processes.[8] An exemplary demonstration is found in the brittle star *Ophiomastix wendtii* (*O.wendtii*), which exhibits light sensitivity capabilities owing to its calcitic microlenses formed through the transformation from ACC to a crystalline structure.[9] Previous studies on the *O.wendtii*'s micro- and nanostructure discovered that the optical lenses' calcite single crystals present a complex structure integrating Mg-poor matrix and coherent Mg-rich nanometric inclusions.[10,11] These inclusions are not randomly dispersed within the crystalline lenses but rather form an arched-shaped layered arrangement demonstrating periodic distances between Mg-rich and Mg-poor layers. The occurrence of such layered pattern is not unique to the *O.wendtii* and can be seen frequently in nature.[12] Many organisms employ layered structures to resist strains and enhance their mechanical properties. For example, the *Odontodactylus scyllarus* (*O. scyllarus*) dactyl club presents a layered structure with two mechanically distinct regions.[13,14] Another remarkable strategy found in nature involves the utilization of composite materials, which provide structural reinforcement and contribute to enhancing the mechanical properties of living organisms. Nature's intricate structural designs, evident in the nacre in mollusk shell, through the chitin helical fibers of the mantis shrimp and to the stiff feathers of birds, enable the formation of materials with optimized strength and toughness.[13,15,16] The composite layered structures such as those observed in *O. wendtii* and *O. scyllarus*, along with the use of amorphous phases within them, were the inspiration for the development of organic-ACC composites.

Formation of 3D-layered structures has become more common owing to the prevalence of 3D printing, allowing the sequential deposition of layers offering convenience and time efficiency in additive manufacturing process. Owing the growing demand for ceramic materials,

numerous 3D-printing methods specifically for ceramics have been developed.[17] Robocasting, a slurry-based additive manufacturing method, has proved to be one of the simplest and most widely employed techniques for 3D printing for ceramic materials. In robocasting, an externally mixed paste with various viscosities and solid loadings is employed for the printing process. However, robocasting is constrained to pastes exhibiting specific properties: shear-thinning behavior for extrusion, self-support post-printing, controlled agglomeration requiring pre-dispersion, and both binders and dispersants that can be easily removed if a dry 3D-printed model is desired. Robocasting process yields a ceramic green body which typically undergoes a sintering stage designed to remove binders and dispersants, eradicate pores, and fuse the ceramic particles together. An efficient sintering process generally requires heating to temperatures ~50%-75% of the ceramic melting points. For example, alumina, a commonly used ceramic material, has a melting point of 2072˚C while sintering temperatures typically range between 1200-1700˚C.[18–20] The use of $CaCO_3$ in 3D printing is limited, and it is often used as an additive to bio-cements[21,22] and scaffolds[23] due to its low decomposition temperature, limiting its ability to go through classical sintering processes. A primary challenge in 3D printing overall, and especially in the 3D printing of ceramic materials, lies in the interfaces between the printed layers. The interfacial area introduces anisotropy to the printed model and compromises its strength in the direction perpendicular to the stacked layers.[24] Numerous suggestions have been proposed to address surface defects in the layers, including the use of a glue paste[25], the incorporation of additives in the slurry such as silica fume[26], fly ash[27] and nano-SiO_2[28], and the incorporation of polymers.[29] All the proposed solutions necessitate alterations to the layers and structure of the printed model. In this context, we propose the utilization of amorphous ACC powder, allowing aggregation and consolidation of ACC particles through low-temperature diffusion, facilitated by substantial amounts of structural water in the ACC. This approach results in the curability of the rough interface layers during the sintering phase.

Materials and methods

ACC powder preparation

Aqueous solutions of $CaCl_2 \cdot 2H_2O$ (147 g in 1 L), $MgCl_2 \cdot 6H_2O$ (203.31 g in 1 L), and Na_2CO_3 (52.995 g in 0.5 L) at a concentration of 1 M were prepared and cooled overnight at 8˚C. Ratios

of 40/60, 50/50, and 60/40 of Ca:Mg solutions were mixed in a glass beaker for 5 minutes. An equivalent amount of Na_2CO_3 solution was then added to the beaker with active mixing, maintaining a 1:1 ion ratio between CO_{3-2} and (Ca^{+2}+Mg^{+2}). The resulting suspension was swiftly filtered through a Buchner funnel using a grade 5 Whatman filter paper, followed by washing with 600 ml of water and 200 ml of acetone. After maintaining suction for 10 minutes, the filtered powder was dried for 3 hours in a vacuum oven at 25˚C and 0.1 MPa. The dried ACC powder was then immersed in an excess of acetone and stored for up to one week.

Paste preparation with various binders

Stored powder was dried, ground with a mortar and pestle, followed by mixing with a dispersant (comprising commercial corn oil at a fixed ratio of 0.1 ml per 1 g of powder) and a mixture of various organic polymers and ethylene glycol (99.8%, AR, Merck). Four different organic polymers were added in 15% w/w to ethylene glycol: commercially available pure bovine collagen, methylcellulose 15 cPs (Alfa Aesar), methylcellulose 400 cPs (Alfa Aesar), and polymerizable D-(+)-Glucose (99.5%, Sigma-Aldrich). Collagen was added in weight percentages ranging from 5 to 20% w/w. The powder was gradually added to the binder and hand-mixed until a solid, firm paste was obtained. The solids-loading of the mixed paste was always maintained at 65%, meaning 1 g of powder for every 0.6-0.7 ml of dispersant-binder mixture. Subsequently, the pastes were loaded into the printing tubes and centrifuged at a rate of 4000 rpm for 20 minutes to degas.

3D Printing and Post-Processing

3D models were formed using a commercially available Hyrel 3D - Engine-SR printer with two KR2-15 stainless steel extrusion heads comprising 1 mm nozzles. 3D-computer-aided design (3D-CAD) of the printed models was sketched using Fusion 360 (Autodesk) following ASTM C1161 – 18 configuration C.[30] The 3D-CAD was converted into an STL file, which was uploaded to the printer, where it was sliced, and the G-code was written. The G-code was then modified to enable printing with two printing heads, alternating layers. The printed models were then placed in a vacuum oven for low-temperature sintering overnight at 150˚C and at a vaccum level of 0.1 MPa.

Measurements of beam strength

The printed models were prepared following the specifications of configuration C in ASTM C1161 – 18. In this configuration, the specimen dimensions are as follows: length 90 mm,

width 8 mm, and depth 6 mm. Subsequently, the specimen was positioned in a three-point flexure fixture, where the two support beams are free to roll, and the middle bearing remains stationary but can be articulated to align with the model's top surface. The support beam was secured at a specified distance of 80 mm, as outlined in the ASTM standard. Ten printed specimens were then tested, and five results were used, fitting the breakage pattern eligible for calculations, as breakage formed where the pressure was enforced, in the middle of the beam. Calculations were performed using the following equation of the strength in three-point flexure:

$$S = \frac{3}{2} \cdot \frac{PL}{2bd^2} \quad (1)$$

where P is the measured break force (in N), L is the outer support span, b is the specimen width and d is the specimen thickness (in m).

The standard deviation between the measurements was calculated as follows:

$$SD = \sqrt{\left(\frac{\sum_1^n (S-\bar{S})^2}{n-1}\right)} \quad (2)$$

where $\bar{S}$, the mean value of the calculated beam strength, is calculated as follows:

$$\bar{S} = \frac{\sum_1^n S}{n} \quad (3)$$

where n is the number of examined specimens.

The printed specimens were inspected using an Instron 3345 Series Single Column Table testing system, calibrated with an error range of 0.02N.

The Young's modulus and the strain energy were calculated using OriginPro 2019 (OriginLab Corporation, Northampton, MA, USA). *High-Resolution Scanning Electron Microscopy*

The samples were imaged using the Zeiss Ultra-Plus FEG-SEM at 1−2 keV with a working distance of 4-4.2. Energy-dispersive X-ray spectroscopy (EDS) was conducted at 9 keV with an 8.4 working distance.

High-Resolution synchrotron powder X-ray diffraction (HRPXRD)

HRPXRD experiments were conducted on ID22 beamline at the European Synchrotron Research Facility (ESRF) in Grenoble, France. The experiments were carried out at a

wavelength of 0.3542Å . Samples were loaded into quartz capillaries, and their XRD patterns were collected.

Lab X-ray diffraction

The diffraction pattern for the $^{40}/_{60}$CGN15% model powdered sample was obtained using the Rigaku SmartLab 9 kW high-resolution diffraction system, utilizing a wavelength of Cu K-α 1.5406 Å.

Thermogravimetric analysis

Thermogravimetric analysis was conducted using the TGA/DSC 3+ instrument from Mettler Toledo. A ceramic crucible was employed, and a small quantity of powder was added. The powder was subsequently heated to 700˚C under a nitrogen environment.

The calculation of evaporated water during the oven drying stage was carried out as follows:

$$Evaporated\ water_{oven\ drying} = \left(1 - \frac{Water\ in\ ACC\ sample}{Water\ in\ printed\ sample\ (ACC+collagen)}\right) \cdot 100\% \qquad (4)$$

Micro-computed tomography (Micro CT)

Micro computed tomography was performed using the NeoScan N80. A sample of the 3D printed model was affixed to the rotating stage, aligned, and scanned using a 67 kV voltage, and 59 µA power, along with a 0.5 aluminum filter.

Dynamic light scattering (DLS)

The hydrodynamic diameter (Dh) and the polydispersity index (PDI), nanoparticles size distribution) were measured by DLS at a scattering angle of 173˚, utilizing Zetasizer Nano-ZS, Malvern Instruments, Malvern, UK. 0.5g of ACC powders with $^{40}/_{60}$, $^{50}/_{50}$, and $^{60}/_{40}$ Ca/Mg ratios were dispersed in 23ml of acetone for 30 minutes in a bath sonicator. The suspension was then filtered using SRP15 Syringe Filter 17559 to avoid the passage of agglomerates. The suspension was rapidly measured after mixing, in a quartz cuvette.

Results and discussion

ACC pastes used in this research were prepared based on a protocol previously described by our group. [8] Ethylene glycol (EG) was chosen as the base binder owing to its non-toxic behavior and ability to preserve the amorphous nature of the ACC powder over time. Various

natural additives were incorporated into EG in a 15% w/w ratio, resulting in the formulation of 50/50 printable pastes. The additives included collagen ($^{50}/_{50}$CGN15%), glucose ($^{50}/_{50}$Glu15%), methylcellulose 15 cPs ($^{50}/_{50}$MCL_15), and methylcellulose 400 cPs ($^{50}/_{50}$MCL_400). Addition of collagen was subsequently studied by mixing ACC Ca/Mg 50/50 powder with 5% w/w in EG ($^{50}/_{50}$CGN5%), 10% w/w in EG ($^{50}/_{50}$CGN10%), and 20% w/w in EG ($^{50}/_{50}$CGN20%). Two additional pastes were formed, one using ACC Ca/Mg $^{60}/_{40}$ powder with 15% w/w of collagen in EG ($^{60}/_{40}$CGN15%), and another with ACC Ca/Mg $^{40}/_{60}$ powder with 15% w/w of collagen in EG ($^{40}/_{60}$CGN15%). Organics-ACC pastes were formed by combining the additive-rich EG solution with ACC powder, resulting in a high solid-loading of approximately 65% ACC. The pastes were then used to print beams measuring 90 mm in length, 8 mm in width, and 6 mm in height. Subsequently, they were dried in a vacuum oven overnight and sintered (150˚C, 0.1 MPa, 15 h). The resulting dry composite models comprised an ACC reinforcement and an organic matrix. Models with a 20% w/w ratio consisted of a composite composed of 93% reinforcement and 7% matrix, models with a 15% w/w ratio consisted of a composite composed of 94.75% reinforcement and 5.25% matrix, models with a 10% w/w ratio consisted of a composite composed of 96.5% reinforcement and 3.5% matrix, and models with a 5% w/w ratio consisted of a composite composed of 98.25% reinforcement and 1.75% matrix.

The morphology and crystallization state of the models was then tested, as depicted in *Figure 1*. The spherical morphology of the ACC was retained after the sintering step (*Figure 1* A-H) in all 3D-printed models. HPXRD diffractograms confirmed that all models remained amorphous (*Figure 1I*). The diffraction peaks in *Figure 1I* stem from NaCl byproducts. The addition of organic matrices to all three ACC powders (with Ca/Mg ratios of $^{50}/_{50}$, $^{60}/_{40}$, and $^{40}/_{60}$) allowed increased stabilization of the ACC's amorphous nature, exceeding two years when stored in ambient conditions.

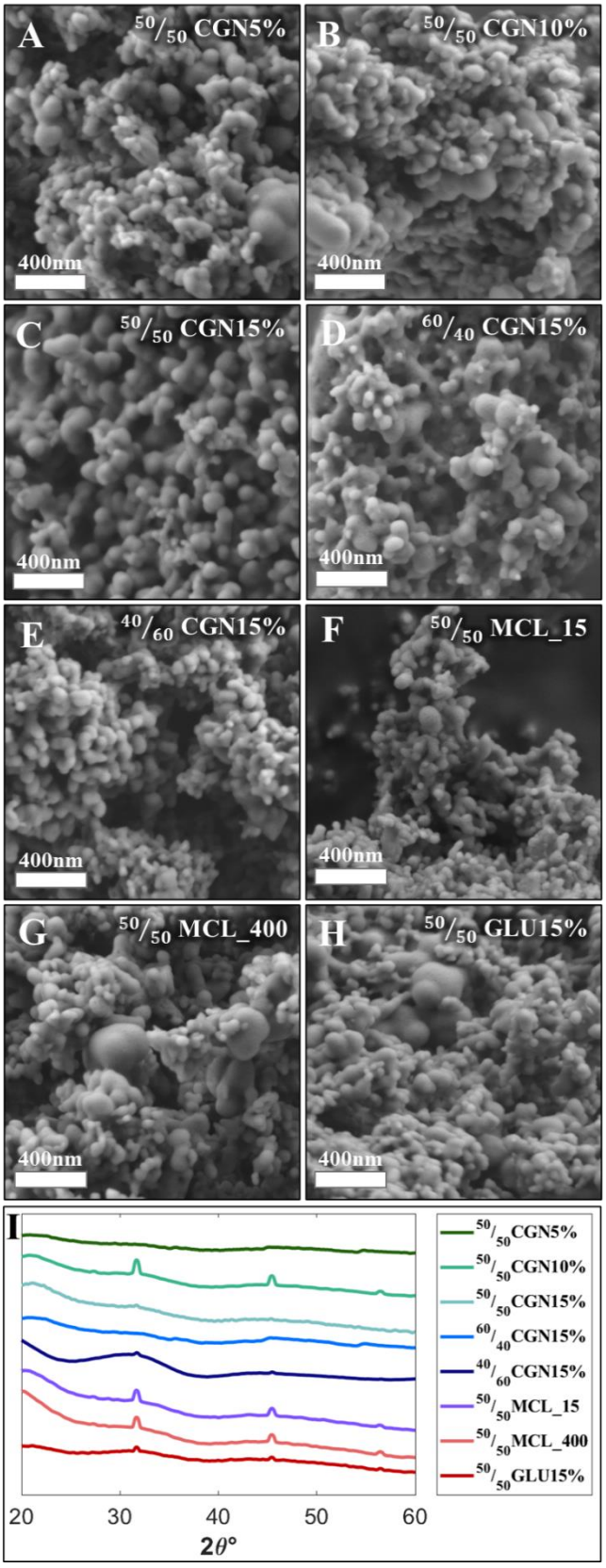

Figure 1 - (A-G) HR-SEM images depict ACC 3D-printed models with various additives after sintering. ACC powders with additive-rich environments are shown as follows: (A) 50/50CGN5%; (B) 50/50CGN10%; (C) CGN 15%w/w where ACC is of 60/40 powder; (E) CGN 15%w/w where ACC is of 40/60; (F) MCL15 15%w/w; (G) MCL400 15%w/w and (H) GLU 15%w/w. (I) HRPXRD patterns at a wavelength of 0.3542Å.

To assess the beam strength (BST) under ambient conditions, the printed models underwent a three-point bending (3PB) test following ASTM 1161 – 18, configuration C. The beam dimensions were as follows: length 90 mm, width 8 mm, and depth 6 mm, with an inner span of 80 mm. Initially, 50/50 ACC powder models with a 15% w/w additive-rich EG solution were tested and compared. Calculations were conducted according to equations (1)-(3) as described in the Materials and Methods section. As depicted in *Figure 2*, $^{50}/_{50}$CGN15% exhibited the highest BST compared to $^{50}/_{50}$MCL_15, $^{50}/_{50}$MCL_400, and $^{50}/_{50}$GLU15%. Based on the outstanding results obtained from the $^{50}/_{50}$CGN15% model, further steps were taken.

First, various CGN concentrations were tested, ranging from 5 to 20% w/w. The $^{50}/_{50}$CGN20% model was omitted due to a plateau observed in the mechanical properties (*Figure S1*). Models with CGN concentrations of 5-15% w/w demonstrated increased BST with higher CGN content in the $^{50}/_{50}$CGN15% model.

Additionally, as CGN 15%w/w additive retained exhibiting the most superior mechanical properties, it was combined with Ca/Mg $^{60}/_{40}$powder ($^{60}/_{40}$CGN15%) and Ca/Mg $^{40}/_{60}$ powder ($^{40}/_{60}$CGN15%). The mechanical strength of the $^{60}/_{40}$CGN15% printed model was further enhanced, conversely, fusion with Ca/Mg $^{40}/_{60}$ powder led to diminished mechanical strength compared to $^{50}/_{50}$CGN15%. Among the tested models, and in the CGN series specifically, $^{60}/_{40}$CGN15% presented the most superior mechanical properties. This result is contrary to what occurs in nature where higher concentration of Mg-rich inclusions in a crystalline $CaCO_3$ structure resulted in higher strength compared to lower-Mg content crystalline $CaCO_3$.[10] Additive-free EG models have been tested as well yet were deemed unsuitable, as they yielded unmeasurable results. These models fractured upon the slightest contact between the pressing bearing and the model, indicating a flexural strength below the measurable 0.006 MPa.

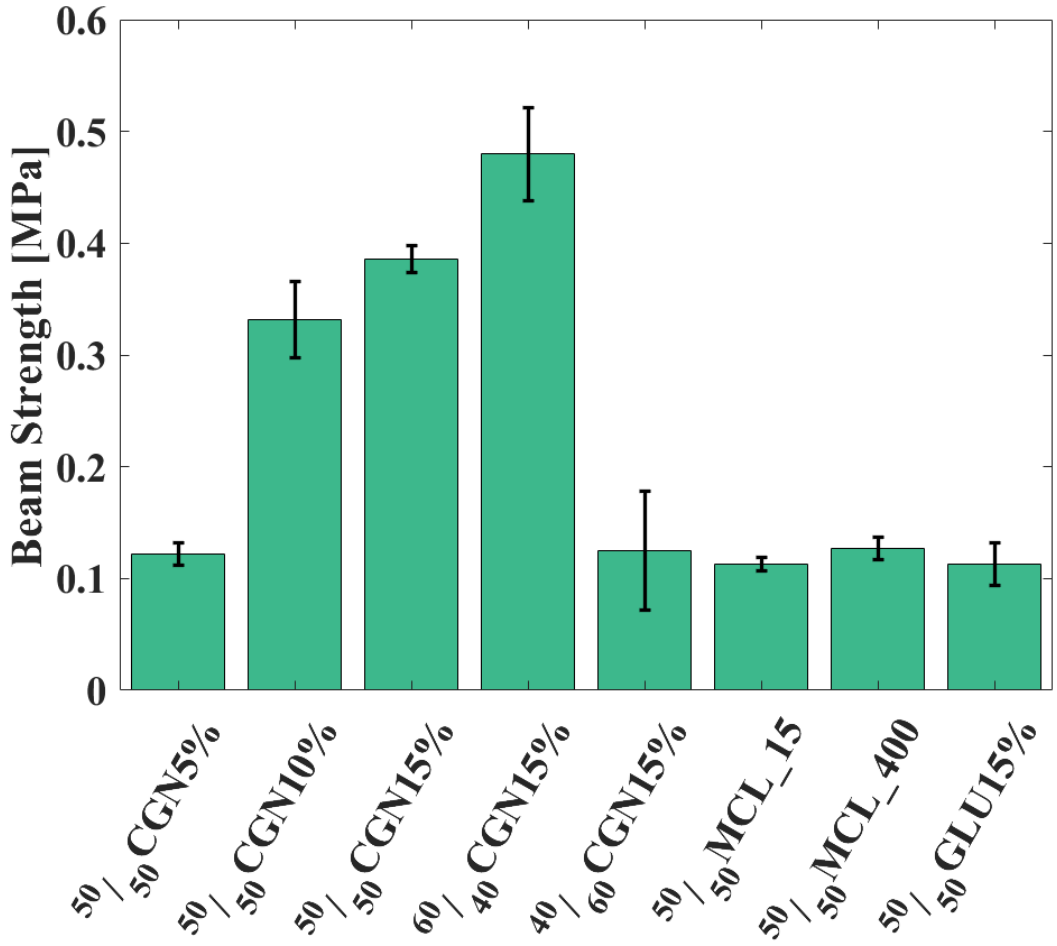

Figure 2 -BST of organics-ACC models with single-material matrix. $^{60}/_{40}$*CGN15% presents the highest BST.*

For a comprehensive understanding of the ACC powder composition dependency (Ca/Mg ratios of $^{40}/_{60}$, $^{50}/_{50}$and $^{60}/_{40}$), the presence of entrapped structural water in the amorphous structure was analyzed using thermogravimetric analysis (TGA). *Table 1* illustrates TGA results revealing the changes in Ca/Mg $^{50}/_{50}$, $^{60}/_{40}$ and $^{40}/_{60}$ ACC powders and their corresponding collagen 15%w/w models $^{50}/_{50}$CGN15%, $^{60}/_{40}$CGN15%, and $^{40}/_{60}$CGN15% occurring between 25 and 600 ˚C . The results obtained from the ACC powders, indicate the amount of structural water entrapped within each powder: 18.77% in the case of $^{40}/_{60}$ ACC powder, 37.39% in the case of $^{50}/_{50}$ ACC powder, and 48.87% in the case of $^{60}/_{40}$ ACC powder. During the initial heating stage (50-150 ˚C), the ACC powder retains its amorphous state while structural water evaporates, leaving behind dry ACC. Around 400˚C, crystallization occurs, accompanied by minimal removal of structural water, aligning with findings from previous studies.[31] The amount of incorporated Mg in the ACC directly correlates with the structural water content; the lower the level of incorporated Mg in the ACC, the higher the structural water content. Following the oven drying process the structural water content

measured at 9.94% for $^{40}/_{60}$CGN15%, 23.33% for $^{50}/_{50}$CGN15%, and 20.14% for $^{60}/_{40}$CGN15%. The percentage of evaporated water during the oven drying stage was calculated as outlined in equation (4). During this process, 47.04% , 37.6% and 58.79% of the water evaporated in the $^{40}/_{60}$CGN15%, $^{50}/_{50}$CGN15% and in the $^{60}/_{40}$CGN15%models, accordingly. The highest strength observed in the $^{60}/_{40}$CGN15% (*Figure 2*) is attributed to the combination of a larger initial water quantity present in the $^{60}/_{40}$ ACC powder and, consequently, a greater amount of water evaporated during the oven drying process (*Table 1*). This effect is most probably a result of water-enhanced diffusion in the $^{60}/_{40}$CGN15%.

The higher amount of structural water released during the drying process of $^{60}/_{40}$CGN15% may also contribute to enhanced aggregation and consolidation of the ACC particles, resulting in a more uniform 3D printed model. The latter effect could also influence the final BST. The influence of Mg concentration on the amount of structural water is still unknown, yet the impact of both Mg and water on the crystallization has been previously studied.[32] While Mg stabilizes the amorphous state of ACC, water accelerates the crystallization process. It has been assumed that the structural water bound to Mg ions increases the stability of Mg-ACC.[33] This assumption, however, contradicts our results.

Table 1. The quantities of evaporated water during the low-temperature sintering in 3D-printing, calculated from TGA analysis, for the pure ACC powders of both $^{50}/_{50}$, $^{60}/_{40}$ and $^{40}/_{60}$ ratios, and the corresponding organic-ACC composites.

Sample	Structural water [%]	Water in the tested sample [%]	Evaporated water during oven drying process [%]
$^{40}/_{60}$ ACC powder	10.99 (initial) 7.88 (crystallization)	18.77	47.04
$^{40}/_{60}$CGN15% model	7.22 (initial) + 2.72 (crystallization)	9.94	
$^{50}/_{50}$ACC powder	28.26 (initial) + 9.13 (crystallization)	37.39	37.6
$^{50}/_{50}$CGN15% model	15.92 (initial) + 7.41 (crystallization)	23.33	
$^{60}/_{40}$ACC Powder	45.32 (initial) + 3.55 (crystallization)	48.87	58.79

$^{60}/_{40}$CGN15% model	11.83 (initial) + 8.31 (crystallization)	20.14

To follow the variations in aggregation and consolidation between the ACC powders, DLS measurements were performed for the $^{40}/_{60}$, $^{50}/_{50}$ and $^{60}/_{40}$ ACC powders as well as for their corresponding collagen 15w/w% models: $^{40}/_{60}$CGN15%, $^{50}/_{50}$CGN15% and $^{60}/_{40}$CGN15% *(Table 2).* As can be seen from the results, the size of powdered ACC ranges between 4-7 nm for all samples before the low-temperature sintering step, and an increase in particle size can be observed as the Mg amount decreases. This observation suggests that aggregation and consolidation process is more prevalence at lower Mg content, corresponding to the increasing amount of evaporated structural water. The obtained PDI is higher than expected for a monodispersed distribution in all samples, which can be explained by the instability and tendency of the powders to agglomerate.[34]

Table 2 – DLS measurements of ACC and 3D printed models, illustrating changes in particle's size before and after oven drying stage.

Sample	Particle size (nm)	PDI	Fold change
$^{40}/_{60}$ ACC powder	6.85±0.59	0.64	7.46
$^{40}/_{60}$CGN15% model	51.15±5.55	0.47	
$^{50}/_{50}$ ACC powder	4.62±0.91	0.34	51.49
$^{50}/_{50}$CGN15% model	237.90±58.08	1	
$^{60}/_{40}$ ACC Powder	4.27±1.34	0.24	64.19
$^{60}/_{40}$CGN15% model	274.10±74.26	0.86	

Based on the obtained results, two case studies of bio-inspired layered structures have been considered. The first case-study, inspired by the Mg distribution in the *O. wendtii* brittle star, involves layering of ACC powders with varying Mg content in a fashion similar to the naturally occurring distribution.[10,11] Mg content variations was achieved using two different pastes, $^{50}/_{50}$CGN15% and $^{60}/_{40}$CGN15%. Layering Patterns (LP) can be seen in *Figure 3 A-C*. The second case-study involves the formation of alternating layers exhibiting low and high Young's modulus inspired by the *O. scyllarus* dactyl club.[13] The layering was achieved using $^{50}/_{50}$CGN15% and $^{50}/_{50}$CGN5% pastes layered in a fashion similar to the naturally occurring distribution, layering can be seen in *Figure 3 D-F*. A printed sample can be seen in *Figure 3 G-H*.

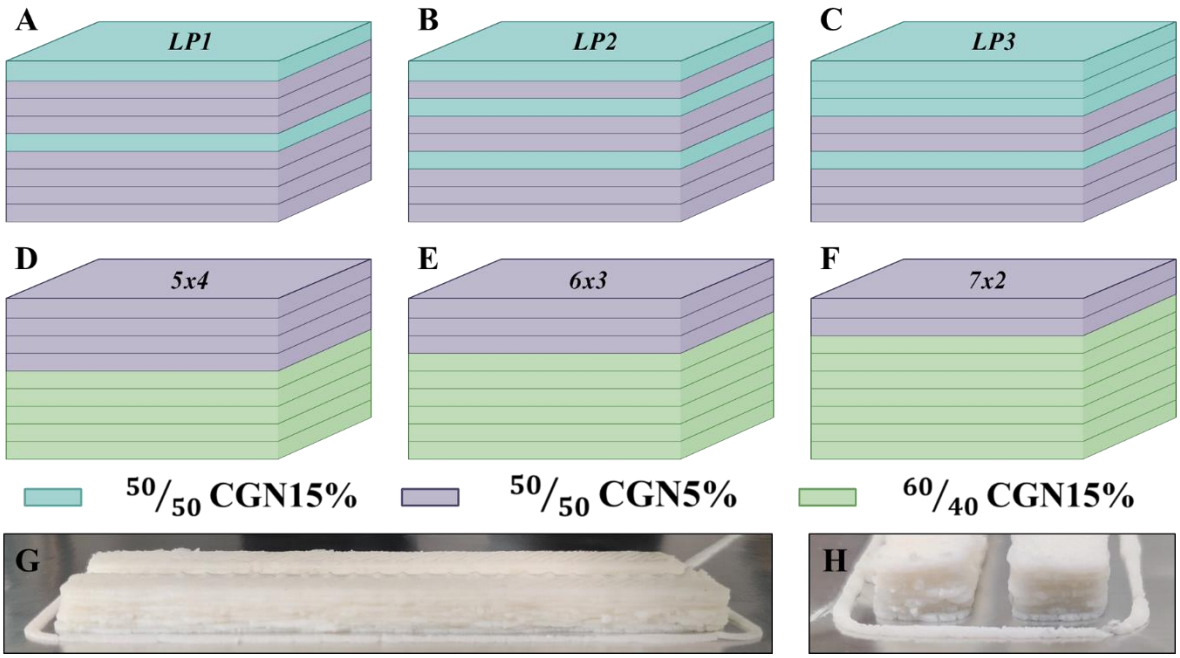

Figure 3 - (A-C) CGN15 and CGN15' tested layered structures, inspired by the o. wendtii brittlestar. (D-F) CGN5 and CGN15 layered structure inspired by the o. scyllarus dactyl club (G-H) a printed sample.

Mechanical measurements of the first case-study layered structures (*Figure 4 A-C*), revealed that by layering $^{50}/_{50}$CGN15% and $^{60}/_{40}$CGN15% the Young's modulus increases compared to the original $^{50}/_{50}$CGN15% model and peaks at a LP ratio defined by LP2 (*Figure 3B)*. LP2 is the one most closely following the strengthening Mg inclusions distribution in the *O. wendtii* where the gap between the first two $^{60}/_{40}$CGN15% layers, compared with the gap between the first and the farthest $^{60}/_{40}$CGN15% layers is ~0.25 [11]. LP2 BST measurements are of the same value as $^{60}/_{40}$CGN15% models. The difference in the strain energy is within the error range. LP2 mechanical properties slightly improve compared to $^{60}/_{40}$CGN15%, indicating the importance of layering of mechanically different layers, and their placement. Mechanical measurements of the second case-study layered structures (*Figure 4 D-F*), revealed that by increasing the ratio of $^{50}/_{50}$CGN15% layers to $^{50}/_{50}$CGN5% layers, the Young's modulus increases and then lowers to a value similar to $^{50}/_{50}$CGN15% with a maximum in the 6x3 layered structures. As the layers of $^{50}/_{50}$CGN15% increases the BST increases, reaching the value of $^{50}/_{50}$CGN15% at 5x4 layered structure. The strain energy values also increase, where 5x4 layered structure strain energy exceeds that of $^{50}/_{50}$CGN15%. The aforementioned results indicate that 5x4 and 6x3 layered structures result in similar or enhanced results compared to the $^{50}/_{50}$CGN15% model. The *O. scyllarus* dactyl club presents a ratio of 0.38 between the region with highest Young's modulus and the entire dactyl club. [13] Due to printing

limitations, the exact ratio between the $^{50}/_{50}$CGN15% layers and the overall layers cannot be reached, it lies between 6x3 and 5x4 (ratios of 0.33 and 0.44 respectively). The layered structures, do not fall short of the $^{50}/_{50}$CGN15%, with less organic matrix in the final product.

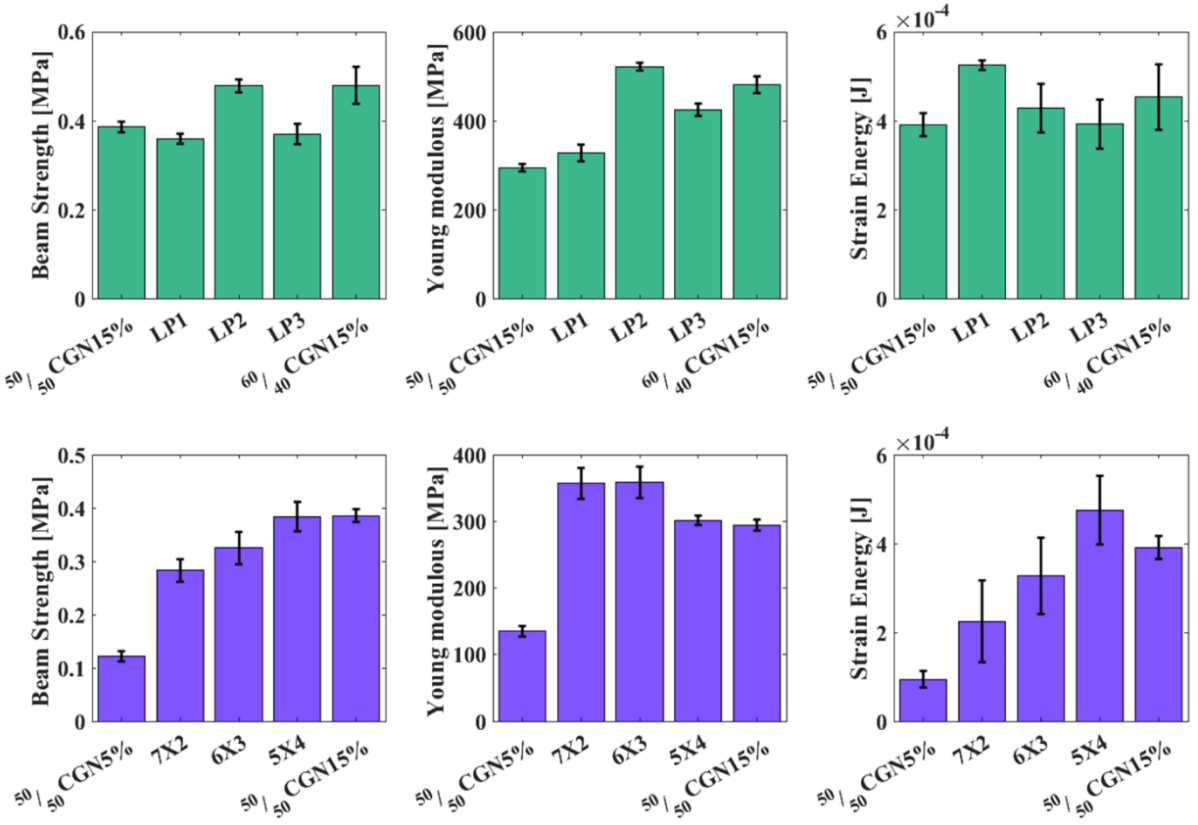

Figure 4 - Mechanical properties of O. wendtii (A-C) and O. scyllarus (D-F) inspired models. (A) BST measurements (B) Young modulus and (C) strain energy graphs of CGN15 and 60/40CGN15% models dispersed in various layered structures. (D) BST measurements (E) Young modulus and (F) strain energy graphs of 50/50CGN5% and CGN15 models dispersed in various layered structures.

Reviewing the breakage surface of the 3D printed models revealed that while one of the most common defects and failure points of 3D printed models is the interface between the layers, layering was not visible at the breaking point of the aforementioned models.[24] In ceramics, to overcome the interface defects and to encourage particle coarsening, high-temperature sintering process is applied. $CaCO_3$ is unable to go through traditional sintering process as calcite, its most stable phase decomposes to CaO and CO_2 at 825˚C, a temperature lower than the temperature required to enable sintering.[31,35] Another limitation is the presence of organics, which burns at ~300˚C, limiting the temperature even further. During the low-temperature sintering step, two processes occur: first, EG and oil evaporate while the ACC particles move towards each other due to degradation of the organic matrix, resulting in a dry composite composed mainly of inorganic ACC aggregates and a small number of organics; second, ACC-particles consolidate due to short-range diffusion in the near-interface regions

resulting in a continues bulk material. Such diffusion is probably enabled due to a rather large amount of structural water in the ACC particles. The use of ACC allows the release of structural water enabling low-temperature sintering. In *Figure 5A* a breakage surface of the LP2 sample, resulting from a 3PB measurement can be seen. Layering defects are not visible except for one highlighted in a purple square, the surface of a lower layer was not covered due to an air bubble in the printing piston deposited in the layer above it. The Ca/Mg distribution in LP2 were measured using EDS and can be seen in *Figure 5B*, these changes in distribution reflect the diffusion occurring during the drying process resulting in a fluctuating curve. In *Figure 5C* a breakage surface of the LP3 sample can be seen. While defects are visible, they are not continuous and are not considered as layering defects. The Ca/Mg distribution in LP3 can be seen in *Figure 5D*, Higher Mg concentration is seen in the $^{50}/_{50}$CGN15% layers compared to the $^{60}/_{40}$CGN15% layers, a distinct step around the location where the different layers interact is visible, implying that the changes at this point and at the interfaces between the different layers in LP2 relates to the aggregation and consolidation processes.

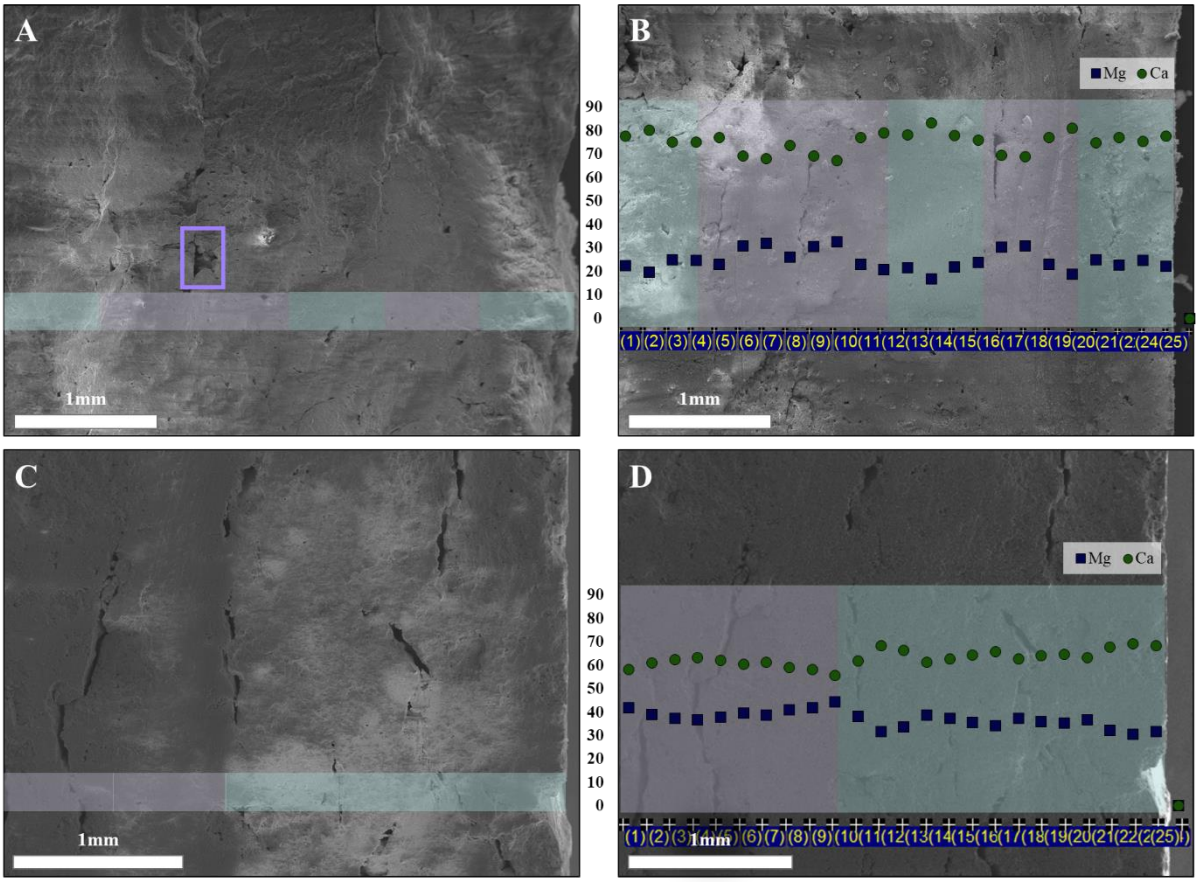

Figure 5 - (A) breakage surface of LP2 sample, resulting from a 3PB measurement. (B) EDS measurement LP2. (C) breakage surface of LP3 sample, resulting from a 3PB measurement. (D) EDS measurement LP3. Green circles – Ca ions, Purple squares – Mg ions. Colored line represents the layered structure according to LP2and LP3, light blue –layers $^{60}/_{40}$CGN15% and purple –.$^{50}/_{50}$CGN15%

Layers' uniformity was further investigated using Neoscan80 microCT, a piece of $^{60}/_{40}$CGN15% and a piece of LP2 3D printed models have been imaged and are depicted in *Figure5 A-D*. In the case of $^{60}/_{40}$CGN15% (*Figure 5A-B*) a bulk like formation can be seen, while both pores and cracks are observed, none of them trace the deposited layers. In the case of LP2 (*Figure 5C-D*) a change in the layers' density is observed, corresponding with the Mg content of each layer, lighter, with lower Mg content, corresponding to $^{60}/_{40}$CGN15% layers, and darker corresponding to $^{50}/_{50}$CGN15% layers. Though the change between the layers is visible, the interface displays as a continues bulk and no interlayer defect can be seen. Cracks and pores can be seen going through the different layers and not centering around the layer's interfaces. Both cases further strengthen the claim of interlayer aggregation and consolidation process around the layers' interfaces.

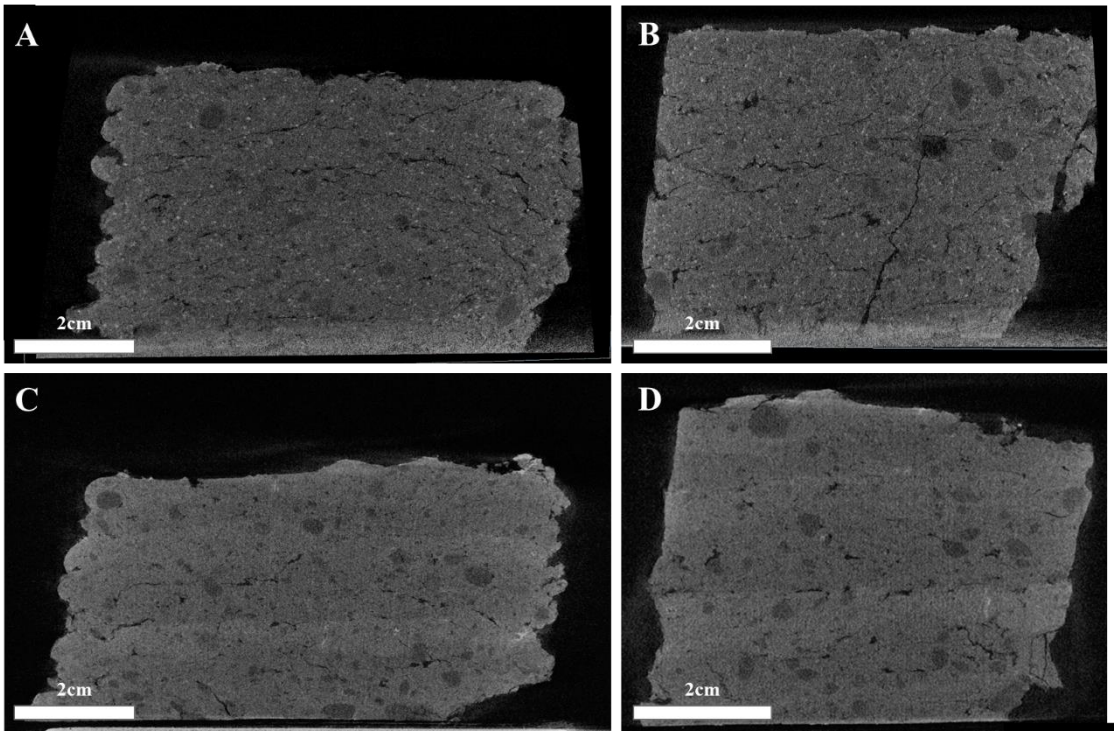

Figure 6 - MicroCT imaging of 60/40CGN15% model (A) front and (B) side view and LP2 model (C) front and (D) side view.

Conclusions

In this study, a bio-inspired approach for 3D-printing ACC composites was presented, following naturally occurring layered structures and utilizing bio-degradable composites. Stabilized ACC powder was further stabilized for long periods of time, exceeding two years, in ambient conditions by introducing organic surroundings as a matrix, similar to what is seen in nature. The resulting composite was composed of high amounts of ACC reinforcement

(>94%) and a small amount of the aforementioned organic matrix. The results obtained highlight the importance of the organic matrix, even in small amounts, for both the stabilization and the mechanical properties of the printed models. Printing of layered structures composed of different ACC reinforcements, inspired by those of the *O. wendtii* optical lenses and the *O. scyllarus* dactyl club revealed that while layering lower-strength materials in a specific manner with materials that possess higher strength, no deterioration of mechanical properties is received. The use of an amorphous phase overcame a long-standing problem common in 3D printing, failure at the inter-layer interfaces. The use of ACC and its ability to perform aggregation and consolidation processes, due to structural water-induced diffusion at relatively low temperatures, resulted in a continuous bulk of the printed model, resembling the formation of single crystalline organs in nature. This bio-inspired layered 3D-printing approach ratified the importance of layering for the mechanical properties of a structure. The use of ACC proved to overcome one of the most burning issues in 3D printing and may offer a new approach for 3D printing of powdered and ceramic materials.

References

[1] S. Weiner, L. Addadi, Crystallization pathways in biomineralization, Annu Rev Mater Res 41 (2011) 21–40. https://doi.org/10.1146/annurev-matsci-062910-095803.

[2] S. Weiner, J. Mahamid, Y. Politi, Y. Ma, L. Addadi, Overview of the amorphous precursor phase strategy in biomineralization, Front Mater Sci China 3 (2009) 104–108. https://doi.org/10.1007/s11706-009-0036-x.

[3] E. Beniash, J. Aizenberg, L. Addadi, S. Weiner, Amorphous calcium carbonate transforms into calcite during sea urchin larval spicule growth, Proc R Soc Lond B Biol Sci 264 (1997) 461–465. https://doi.org/10.1098/rspb.1997.0066.

[4] L. Addadi, S. Raz, S. Weiner, Taking Advantage of Disorder: Amorphous Calcium Carbonate and Its Roles in Biomineralization, Advanced Materials 15 (2003) 959–970. https://doi.org/10.1002/adma.200300381.

[5] S. Raz, S. Weiner, L. Addadi, Formation of High-Magnesian Calcites via an Amorphous Precursor Phase: Possible Biological Implications, Advanced Materials 12 (2000) 38–42. https://doi.org/10.1002/(SICI)1521-4095(200001)12:1<38::AID-ADMA38>3.0.CO;2-I.

[6] G. Falini, M. Gazzano, A. Ripamonti, Crystallization of calcium carbonate in presence of magnesium and polyelectrolytes, J Cryst Growth 137 (1994) 577–584. https://doi.org/10.1016/0022-0248(94)91001-4.

[7] Y. Politi, D.R. Batchelor, P. Zaslansky, B.F. Chmelka, J.C. Weaver, I. Sagi, S. Weiner, L. Addadi, Role of Magnesium Ion in the Stabilization of Biogenic Amorphous Calcium Carbonate: A

Structure−Function Investigation, Chemistry of Materials 22 (2010) 161–166. https://doi.org/10.1021/cm902674h.

[8] H. Shaked, I. Polishchuk, A. Nagel, Y. Bekenstein, B. Pokroy, Long-term stabilized amorphous calcium carbonate—an ink for bio-inspired 3D printing, Mater Today Bio 11 (2021) 100120. https://doi.org/10.1016/j.mtbio.2021.100120.

[9] J. Aizenberg, A. Tkachenko, S. Weiner, L. Addadi, G. Hendler, Calcitic microlenses as part of the photoreceptor system in brittlestars, Nature 412 (2001) 819–822. https://doi.org/10.1038/35090573.

[10] I. Polishchuk, A.A. Bracha, L. Bloch, D. Levy, S. Kozachkevich, Y. Etinger-Geller, Y. Kauffmann, M. Burghammer, C. Giacobbe, J. Villanova, G. Hendler, C.Y. Sun, A.J. Giuffre, M.A. Marcus, L. Kundanati, P. Zaslansky, N.M. Pugno, P.U.P.A. Gilbert, A. Katsman, B. Pokroy, Coherently aligned nanoparticles within a biogenic single crystal: A biological prestressing strategy, Science (1979) 358 (2017) 1294–1298. https://doi.org/10.1126/science.aaj2156.

[11] E. Seknazi, S. Kozachkevich, I. Polishchuk, N. Bianco Stein, J. Villanova, J.-P. Suuronen, C. Dejoie, P. Zaslansky, A. Katsman, B. Pokroy, From spinodal decomposition to alternating layered structure within single crystals of biogenic magnesium calcite, Nat Commun 10 (2019) 4559. https://doi.org/10.1038/s41467-019-12168-8.

[12] N. Bianco-Stein, I. Polishchuk, A. Lang, L. Portal, C. Dejoie, A. Katsman, B. Pokroy, High-Mg calcite nanoparticles within a low-Mg calcite matrix: A widespread phenomenon in biomineralization, Proceedings of the National Academy of Sciences 119 (2022). https://doi.org/10.1073/pnas.2120177119.

[13] J.C. Weaver, G.W. Milliron, A. Miserez, K. Evans-Lutterodt, S. Herrera, I. Gallana, W.J. Mershon, B. Swanson, P. Zavattieri, E. DiMasi, D. Kisailus, The stomatopod dactyl club: A formidable damage-tolerant biological hammer, Science (1979) 336 (2012) 1275–1280. https://doi.org/10.1126/science.1218764.

[14] S.N. Patek, R.L. Caldwell, Extreme impact and cavitation forces of a biological hammer: Strike forces of the peacock mantis shrimp Odontodactylus scyllarus, Journal of Experimental Biology 208 (2005) 3655–3664. https://doi.org/10.1242/jeb.01831.

[15] M.A. Meyers, A.Y.M. Lin, Y. Seki, P. Chen, B.K. Kad, S. Bodde, Structural biological composites: An overview, JOM 58 (2006) 35–41. https://doi.org/10.1007/s11837-006-0138-1.

[16] D. Nepal, S. Kang, K.M. Adstedt, K. Kanhaiya, M.R. Bockstaller, L.C. Brinson, M.J. Buehler, P. v. Coveney, K. Dayal, J.A. El-Awady, L.C. Henderson, D.L. Kaplan, S. Keten, N.A. Kotov, G.C. Schatz, S. Vignolini, F. Vollrath, Y. Wang, B.I. Yakobson, V. v. Tsukruk, H. Heinz, Hierarchically structured bioinspired nanocomposites, Nat Mater 22 (2023) 18–35. https://doi.org/10.1038/s41563-022-01384-1.

[17] Z. Chen, Z. Li, J. Li, C. Liu, C. Lao, Y. Fu, C. Liu, Y. Li, P. Wang, Y. He, 3D printing of ceramics: A review, J Eur Ceram Soc 39 (2019) 661–687. https://doi.org/10.1016/j.jeurceramsoc.2018.11.013.

[18] H. Guo, A. Baker, J. Guo, C.A. Randall, Cold Sintering Process: A Novel Technique for Low-Temperature Ceramic Processing of Ferroelectrics, Journal of the American Ceramic Society 99 (2016) 3489–3507. https://doi.org/10.1111/jace.14554.

[19] Y.S. Han, J.B. Li, Q.M. Wei, K. Tang, The effect of sintering temperatures on alumina foam strength, Ceram Int 28 (2002) 755–759. https://doi.org/10.1016/S0272-8842(02)00039-1.

[20] I.B. CUTLER, C. BRADSHAW, C.J. CHRISTENSEN, E.P. HYATT, Sintering of Alumina at Temperatures of 1400oC. and Below, Journal of the American Ceramic Society 40 (1957) 134–139. https://doi.org/10.1111/j.1151-2916.1957.tb12589.x.

[21] C. Nething, M. Smirnova, J.A.D. Gröning, W. Haase, A. Stolz, W. Sobek, A method for 3D printing bio-cemented spatial structures using sand and urease active calcium carbonate powder, Mater Des 195 (2020) 109032. https://doi.org/10.1016/j.matdes.2020.109032.

[22] H. Yang, Y. Che, M. Shi, Influences of calcium carbonate nanoparticles on the workability and strength of 3D printing cementitious materials containing limestone powder, Journal of Building Engineering 44 (2021) 102976. https://doi.org/10.1016/j.jobe.2021.102976.

[23] T. Wang, J. Zheng, T. Hu, H. Zhang, K. Fu, R. Yin, W. Zhang, Three-Dimensional Printing of Calcium Carbonate/Hydroxyapatite Scaffolds at Low Temperature for Bone Tissue Engineering, 3D Print Addit Manuf 8 (2021) 1–13. https://doi.org/10.1089/3dp.2020.0140.

[24] Z. Geng, W. She, W. Zuo, K. Lyu, H. Pan, Y. Zhang, C. Miao, Layer-interface properties in 3D printed concrete: Dual hierarchical structure and micromechanical characterization, Cem Concr Res 138 (2020) 106220. https://doi.org/10.1016/j.cemconres.2020.106220.

[25] T. Marchment, J. Sanjayan, M. Xia, Method of enhancing interlayer bond strength in construction scale 3D printing with mortar by effective bond area amplification, Mater Des 169 (2019) 107684. https://doi.org/10.1016/j.matdes.2019.107684.

[26] V.N. Nerella, V. Mechtcherine, MICRO-AND MACROSCOPIC INVESTIGATIONS ON THE INTERFACE BETWEEN LAYERS OF 3D-PRINTED CEMENTITIOUS ELEMENTS-Project B1 View project Application of Carbon nano tubes in geopolymers View project, (2017). https://www.researchgate.net/publication/319504633 (accessed January 2, 2023).

[27] G. Li, A new way to increase the long-term bond strength of new-to-old concrete by the use of fly ash, Cem Concr Res 33 (2003) 799–806. https://doi.org/10.1016/S0008-8846(02)01064-5.

[28] B.-W. Jo, C.-H. Kim, G. Tae, J.-B. Park, Characteristics of cement mortar with nano-SiO2 particles, Constr Build Mater 21 (2007) 1351–1355. https://doi.org/10.1016/j.conbuildmat.2005.12.020.

[29] D.R. Morgan, Compatibility of concrete repair materials and systems, Constr Build Mater 10 (1996) 57–67. https://doi.org/10.1016/0950-0618(95)00060-7.

[30] ASTM International, C1161-13: Standard Test Method for Flexural Strength of Advanced Ceramics at Ambient, Annual Book of ASTM Standards 11 (2008) 1–16. https://doi.org/10.1520/C1161-13.

[31] N. Bianco-Stein, I. Polishchuk, G. Seiden, J. Villanova, A. Rack, P. Zaslansky, B. Pokroy, Helical Microstructures of the Mineralized Coralline Red Algae Determine Their Mechanical Properties, Advanced Science 7 (2020) 2000108. https://doi.org/10.1002/advs.202000108.

[32] M. Albéric, L. Bertinetti, Z. Zou, P. Fratzl, W. Habraken, Y. Politi, The Crystallization of Amorphous Calcium Carbonate is Kinetically Governed by Ion Impurities and Water, Advanced Science 5 (2018). https://doi.org/10.1002/advs.201701000.

[33] C.-J. Lin, S.-Y. Yang, S.-J. Huang, J.C.C. Chan, Structural Characterization of Mg-Stabilized Amorphous Calcium Carbonate by Mg-25 Solid-State NMR Spectroscopy, The Journal of Physical Chemistry C 119 (2015) 7225–7233. https://doi.org/10.1021/jp512971a.

[34] A.C. Society, M. Id, M. Type, A.D. Submitted, C. List, E.S. Hedderick, M. Science, E. Eyal, E.S. Shimoni, S. Estroff, M. Science, E. Gal, Surface-induced coacervation facilitates localized precipitation of mineral precursors from dilute solutions, (2020).

[35] I. Galan, F.P. Glasser, C. Andrade, Calcium carbonate decomposition, J Therm Anal Calorim 111 (2013) 1197–1202. https://doi.org/10.1007/s10973-012-2290-x.